Su *et al. Microstructures* 2024;4:2024049
DOI: 10.20517/microstructures.2024.18

Microstructures

Research Article

Open Access

Longitudinal zero thermal expansion in Re-Fe (R = Tb, Er) eutectic alloys with high fracture resistance

Jixuan Su, Chengyi Yu, Yili Cao, Qiang Li, Jun Miao, Kun Lin, Xianran Xing

Beijing Advanced Innovation Center for Materials Genome Engineering, and Institute of Solid State Chemistry, University of Science and Technology Beijing, Beijing 100083, China.

Correspondence to: Prof. Kun Lin, Beijing Advanced Innovation Center for Materials Genome Engineering, and Institute of Solid State Chemistry, University of Science and Technology Beijing, No. 30 Xueyuan Road, Haidian District, Beijing 100083, China. E-mail: kunlin@ustb.edu.cn

How to cite this article: Su J, Yu C, Cao Y, Li Q, Miao J, Lin K, Xing X. Longitudinal zero thermal expansion in Re-Fe (R = Tb, Er) eutectic alloys with high fracture resistance. *Microstructures* 2024;4:2024049. https://dx.doi.org/10.20517/microstructures.2024.18

Received: 29 Feb 2024 **First Decision:** 18 Apr 2024 **Revised:** 6 May 2024 **Accepted:** 8 May 2024 **Published:** 10 Aug 2024

Academic Editor: Andrea Sanson **Copy Editor:** Fangling Lan **Production Editor:** Fangling Lan

Abstract

Longitudinal zero thermal expansion (LZTE) alloys hold unique application potentials due to their size stability along the longitudinal direction and thermal expansion compatibility inside the radial plane. However, they are rare and usually exist in an ordered intermetallic phase that suffers from poor mechanical properties. Here, two novel alloys, $Tb_{0.05}Fe_{0.95}$ and $Er_{0.04}Fe_{0.96}$, were designed and fabricated by hypo-eutectic reaction. The $Tb_{0.05}Fe_{0.95}$ alloy possesses axial zero thermal expansion with an ultralow coefficient of thermal expansion (α_l = 0.029 × 10^{-6} K^{-1}, 110 to 425 K) and a large ultimate compressive stress (δ_{US}) of 0.80 GPa with a strain limit of 3.9%, and the $Er_{0.04}Fe_{0.96}$ alloy exhibits axial zero thermal expansion (α_l = -0.33 × 10^{-6} K^{-1}, 110 to 330 K) and an ultimate compressive stress (δ_{US}) of 0.73 GPa with a large strain limit of 13.8%. Further studies show that the [001] axis of the hexagonal R_2Fe_{17} phase (R = Tb, Dy) tends to nucleate and grow along the maximum temperature gradient direction, where the negative thermal expansion of the R_2Fe_{17} phase is neutralized by the positive thermal expansion of α-Fe and leads to the LZTE. The fractured surface shows that the plastic α-Fe phase hinders the enlargement of micro-cracks from the brittle R_2Fe_{17} phase, and it leads to plasticity while the matrix R_2Fe_{17} phase gives rise to high strength. Furthermore, the present LZTE alloys are stable under thermal circulation, which has application prospects for high-precision engineering.

Keywords: Zero thermal expansion, eutectic alloys, high fracture resistance, dual-phase alloys

© The Author(s) 2024. **Open Access** This article is licensed under a Creative Commons Attribution 4.0 International License (https://creativecommons.org/licenses/by/4.0/), which permits unrestricted use, sharing, adaptation, distribution and reproduction in any medium or format, for any purpose, even commercially, as long as you give appropriate credit to the original author(s) and the source, provide a link to the Creative Commons license, and indicate if changes were made.

INTRODUCTION

Zero thermal expansion (ZTE) alloys are vital for high-precision fabrications due to their unique size-invariance property under temperature fluctuations[1-7]. Critical applications exist that call for ZTE in one direction but normal positive thermal expansion (PTE) in other directions, i.e., longitudinal ZTE (LZTE). For example, optic support systems of a space telescope should have an extremely small CTE (coefficient of thermal expansion, $\alpha_l < 1 \times 10^{-6}$ K^{-1}) in the supporting direction to ensure its focus accuracy, but have positive CTEs ($\alpha_l \approx 10 \times 10^{-6}$ K^{-1}) in the radial planes, allowing for compliant mounting of optical elements[8-12]. However, most commercial ZTE alloys are based on a high-symmetric face-centered-cubic (fcc) structure (e.g., the Fe-Ni Invar) with isotropic performances[13-20]. In recent years, several LZTE systems with hexagonal or tetragonal symmetries have been developed, such as Ho_2Fe_{17}, Er-Fe-V-Mo, $ZrFe_2$, *etc.*[20-28]. However, these alloys are generally ordered intermetallic phases that are highly brittle due to their insufficient deformation mechanism and exhibit catastrophic failure under stress. New alloy systems with superior mechanical properties are desirable for developing LZTE devices.

On the R-Fe (R = rare earth) diphasic diagram, R_2Fe_{17} can form a eutectic system with Fe[29] (see Figure 1). Hence, the α-Fe phase and the R_2Fe_{17} phase will coexist to form the natural dual-phase alloy by hypo-eutectic or hyper-eutectic reactions. Interestingly, Fe is a common and low-cost element and among its phases, α-Fe, which has both features of plasticity and isotropic PTE. Meanwhile, R_2Fe_{17} is a representative anisotropic negative thermal expansion (NTE) intermetallic compound with high strength and low plasticity. This provides a possibility to obtain a toughened LZTE alloy if the phase fractions and crystallographic orientation of R_2Fe_{17} and α-Fe phases could be controlled suitably in the dual-phase alloy. As shown in Figure 1, the former property can be reached by adjusting the composition of R_xFe_{1-x} samples through hypo-eutectic or hyper-eutectic reactions, while the latter one can be realized by controlled axial cooling and crystallizing using the electric arc furnace[22].

In this work, the thermal expansion performance was successfully tailored from moderate PTE to desired ZTE and then to NTE in the Tb-Fe and Er-Fe systems. Encouragingly, the LZTE dual-phase alloys with nominal compositions of $Tb_{0.05}Fe_{0.95}$ and $Er_{0.04}Fe_{0.96}$ were designed and synthesized. The alloys have high thermal circulation stability over a wide temperature range covering room temperature, a moderate combination of strength and plasticity, and machinability. The hard R_2Fe_{17} phases are the matrix of the dual-phase alloy, preserving their high strength within it. The plastic α-Fe phase impedes the propagation of microcracks in the R_2Fe_{17} matrix under compression, enhancing the plasticity of the dual-phase alloy. These alloys hold application prospects as LZTE materials in high-precision technology.

MATERIALS AND METHODS

Sample synthesis

The samples of Tb_xFe_{1-x} (x = 0.025, x = 0.05, and x = 0.075, notated as 2.5Tb, 5Tb, and 7.5Tb, respectively) and Er_xFe_{1-x} (x = 0.02, x = 0.04, x = 0.07, and x = 0.09, notated as 2Er, 4Er, 7Er, and 9Er, respectively) were manufactured with nominal compositions in a vacuum arc melting furnace under a high purity argon atmosphere, and, in parallel, the Ti ingot was melted to absorb possible residual oxygen. In order to guarantee homogeneity, the ingots were turned over and melted four times. After that, the samples were annealed at 1,373 K under an argon atmosphere for nearly 24 h and then quenched in liquid nitrogen after the annealing.

Materials characterization

X-ray diffraction (XRD) measurements were carried out using RIGAKU SmartLab 9 kw equipped with a Co-Kα radiation source. Temperature-dependent synchrotron XRD (SXRD) patterns were recorded at the

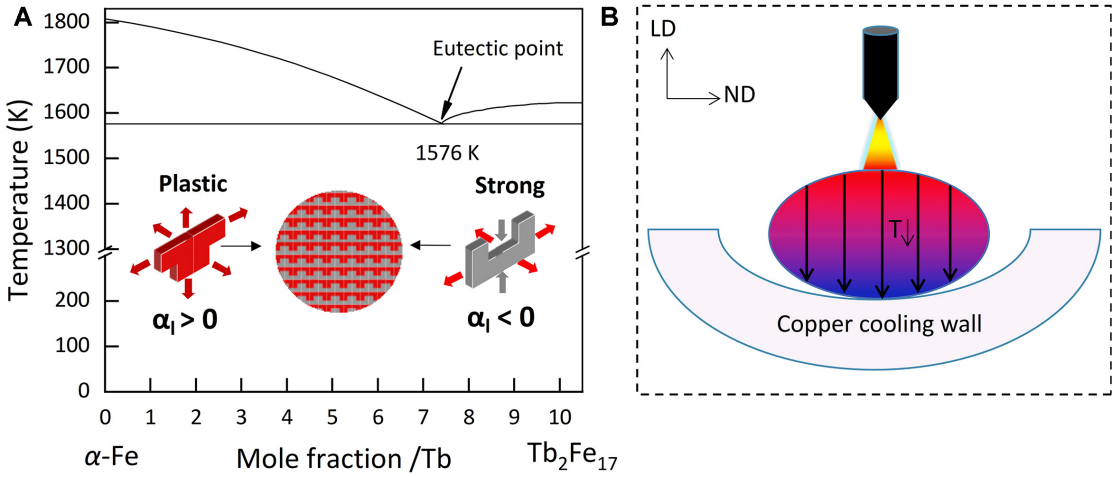

Figure 1. (A) The Tb-Fe phase diagram and design thinking of LZTE alloys with comprehensive properties. (B) Schematic of controlled axial cooling and crystallizing for a dual-phase alloy using the electric arc furnace.

BL44B2 beamline in SPring-8 (λ = 0.69995 Å), Japan. The detailed crystal structure and cell parameters were obtained by Rietveld refinements using the FullProf software. The macroscopic thermal expansion curves (ΔL/L0) were measured by a thermo-dilatometer (NETZSCH DIL402) at a heating rate of 5 K/min over a temperature range of 110-473 K. The thermal cycling test was carried out by an auto-mechanical arm. In every cycle, the samples were soaked in hot water (373 K) for 10 s and then rapidly switched to liquid nitrogen (77 K) for another 10 s. The macroscopic thermal expansion was measured by a dilatometer (NETZSCH DIL402). Mechanical property testing was conducted using a CMT4105 universal electronic compressive testing machine with an initial strain rate of 0.025 s^{-1} at room temperature. The samples for the compression tests were cut to a dimension of Φ 5 mm × 8 mm using electrical discharging wire-cutting and polished using SiC paper. The sample microstructure was determined using a scanning electron microscope (SEM, Zeiss GeminiSEM 500), and composition, including elemental mapping images, was obtained using energy-dispersive spectroscopy (EDS). The microstructure orientation of the sample was obtained by electron backscattered diffraction [TESCAN MIRA 3LMH SEM and Symmetry electron backscattering diffraction (EBSD)], and the EBSD data were analyzed using the Channel 5 software. The magnetization measurements were carried out using a physical property measurement system (PPMS) of Quantum Design with the vibrating sample magnetometer (VSM) and superconducting quantum interference device (SQUID). The phase interface structure of the sample was characterized by high-resolution transmission electron microscopy (HRTEM) and measured by the FEI Titan G260-300 kV transmission electron microscope (TEM).

RESULTS AND DISCUSSION

XRD analysis revealed the crystal structure of targeted samples. It is found that all 2.5Tb, 5Tb and 7.5Tb alloys are dual-phase, composed of α-Fe (labeled as α) and Tb_2Fe_{17} phases (expressed as H) without other detective impurities, while for 2Er, 4Er, 7Er and 9Er alloys, all the peaks belong to the α-Fe or Er_2Fe_{17} phase, agreeing well with the R-Fe phase diagram (see Figure 2A and B). With rising rare earth content, the intensity of peaks corresponding to crystal plane 302(H) gradually increases, while that corresponding to crystal plane 110(α) gradually decreases. It means that the content of the H phase augments, and that of the α phase declines (see Figure 2C). In addition, the Rietveld refinement of XRD results for samples verifies an approximately linear evolution with Tb/Er mole fractions in these dual-phase alloys (see Figure 2D, the full-profile fitting patterns for 2.5Tb, 5Tb and 7.5Tb alloys, see Supplementary Figure 1 and 2Er, 4Er, 7Er and

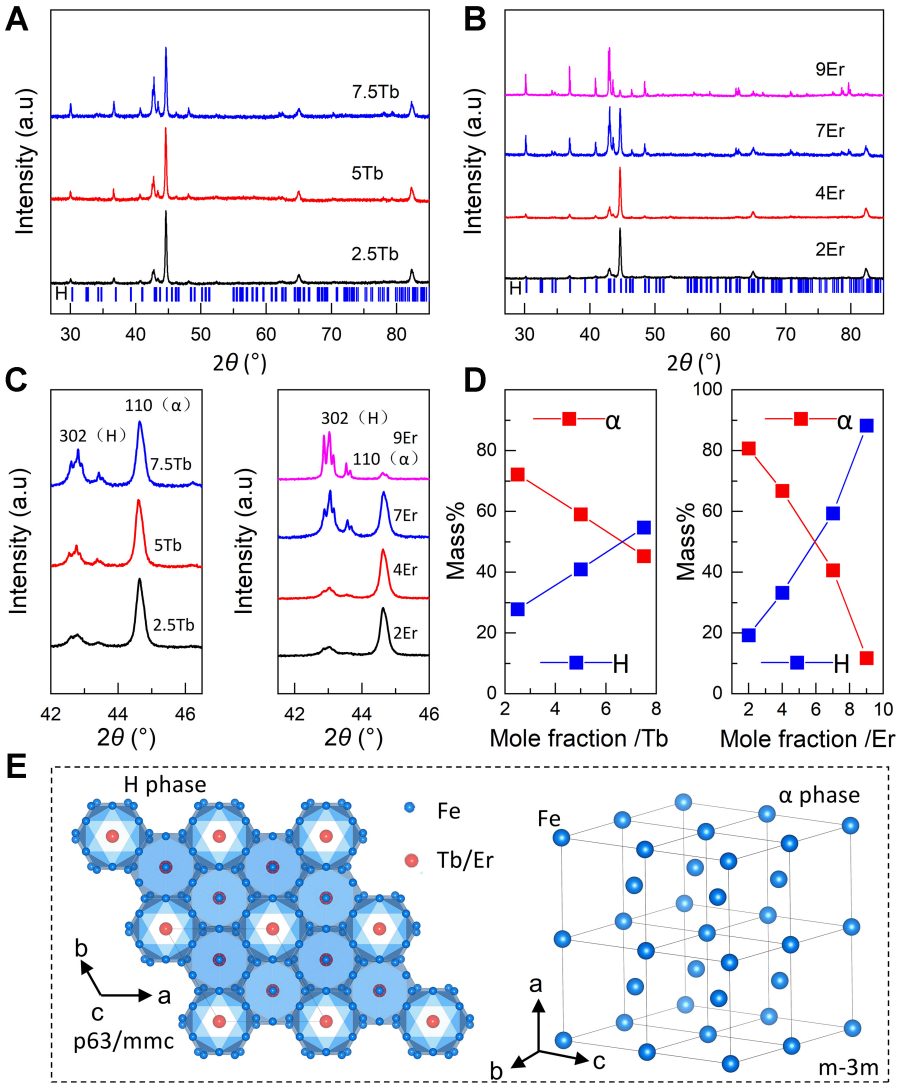

Figure 2. Phase and crystal structure. (A-C) X-ray diffraction for 2.5Tb, 5Tb, 7.5Tb and 2Er, 4Er, 7Er, 9Er alloys, respectively. (D) The ratio of H and α phases in samples obtained by Rietveld refinement. (E) Crystal structures of H and α phases.

9Er alloys, see Supplementary Figure 2. The crystal structures of the H and α phases refined by XRD data are shown in Figure 2E. In the structure of the hexagonal phase, the Tb/Er atom and the Fe atom occupy sites 2b (0,0,1/4), 2d (1/3,2/3,3/4), 2c (1/3,2/3,1/4) and sites 4f (1/3,2/3,z), 6g (1/2,0,0), 12j (x,y,1/4), 12k (x,2x,z), respectively. The H phase adopts a Th_2Ni_{17}-type structure (space group: $P6_3/mmc$) with cell parameters of a = 8.4583 ± 0.01 Å, c = 8.3005 ± 0.01 Å, V = 514.28 ± 0.03 Å^3 while the α phase adopts a body-centered-cubic phase (space group: Im-3m) with cell parameters a = 2.8387 ± 0.01 Å, V = 22.87 ± 0.02 Å^3 and the Fe atom occupy site 2a (0,0,0). The XRD results indicate that the design idea of regulating the two-phase ratio of the alloys by controlling the chemical ratio of the samples was successfully realized.

To explore the morphology and phase distribution of the dual-phase alloys, SEM and EBSD measurements were carried out. Due to the similarity of these alloys, we systematically studied only the microstructure of the 5Tb alloy, as shown in Figure 3A-F. As to the microstructure of the 4Er alloy, refer to Supplementary Figure 3. The SEM images and element mapping inside the TD (transverse direction)-ND

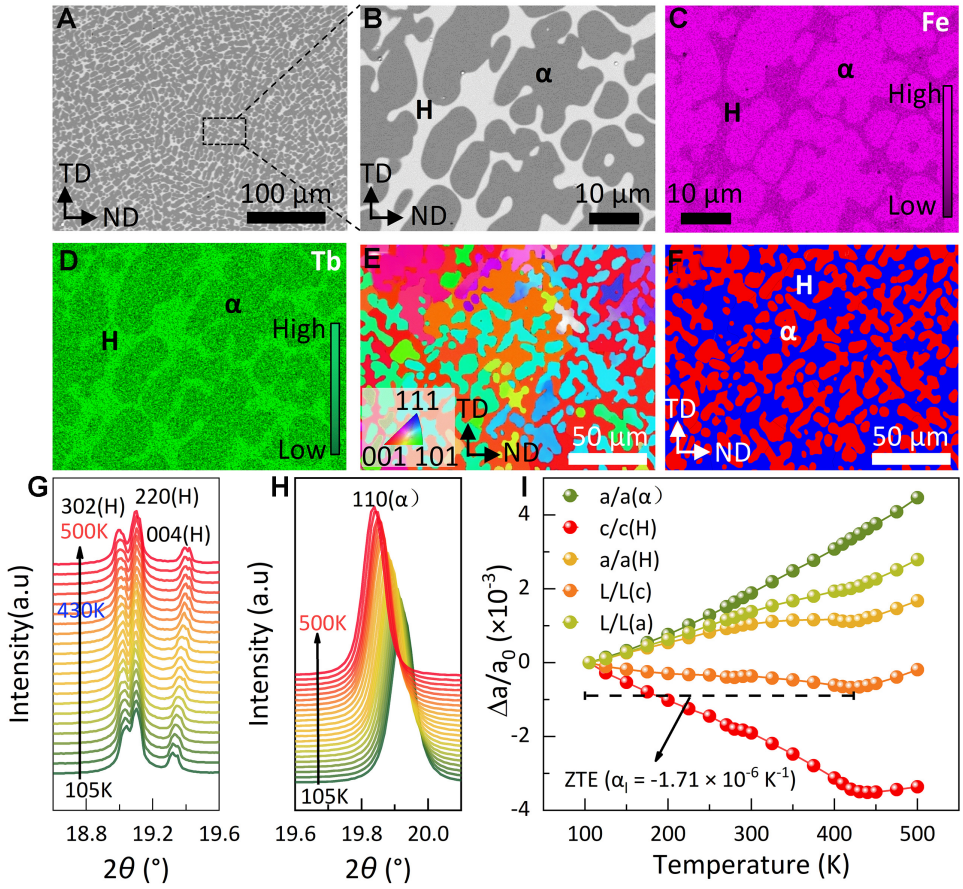

Figure 3. Microstructure of the 5Tb alloy. (A) The morphology of the 5Tb alloy was measured by scanning electron microscope (SEM) in the TD (transverse direction) - ND (normal direction) plane. (B) The enlarged region in (A) is marked by a dotted rectangle. (C and D) Element mappings of Fe (C) and Tb (D) corresponding to the region shown in (B). (E) Electron backscattered diffraction (EBSD) inverse pole figures of crystal orientation for the 5Tb alloy in the TD-ND plane. (F) EBSD phase figure for the 5Tb alloy. (G and H) Temperature-dependent synchrotron X-ray diffraction for 5Tb. (I) Lattice thermal expansions of H in the *a* and *c* axes, α in the *a* axis. L(*a*) and L(*c*) represent the average "lattice length" of the two phases in the LD and TD-ND plane, respectively.

(normal direction) planes show that the dendritic lamellar α phase (in dark, 10-100 μm) is homogeneously dispersed in the continuous H phase matrix (in gray, 50-100 μm, see Figure 3A-D), which is mutually confirmed with the XRD results. Above all, the EBSD inverse pole figure (IPF) of 5Tb indicates that the crystal orientations of H and α phases are highly consistent along the longitudinal direction (LD) (the EBSD pole figures of 5Tb alloy, see Supplementary Figure 4). It suggests the existence of crystallographic texture along the LD for both the H and α phases ([001]H//[111]α//LD), as seen in Figure 3E and F. This phenomenon results from the huge temperature gradient from the melt to the copper cooling wall during the crystallization of bulk materials[20]. (The Pictures in Supplementary Figure 5 show a huge temperature gradient). It provides a basis for manipulating the uniaxial ZTE due to the anisotropic nature of the H phase.

The existence of crystallographic texture of the H phase manifests that the uniaxial ZTE could be reached if the NTE of H along the c axis compensates for the PTE of α along the a axis. Thus, temperature-dependent SXRD for 5Tb was performed to reveal the lattice thermal expansion behaviors (see Figure 3G-I). Obviously, the 110(α) peak gradually shifts to lower angles as the temperature increases. This shows a broadening in the spacing of the 110(α) crystal planes and an expansion in the lattice constant for the α

phase. Likewise, the 302(H) and 220(H) peaks gradually move to lower angles with the temperature elevation, which corresponds to the expansion of interplanar spacing inside the basal a-b plane for the H phase. More importantly, the 004(H) peak obviously shifts to higher angles with temperatures over 105-430 K, suggesting the contraction of the c axis. This peak moves back to lower angles when the temperature is further increased above 430 K (the magnetic Curie temperature, see Supplementary Figure 6A). As shown in Figure 3I, the lattice thermal expansions are α_a = 3.3 × 10^{-6} K^{-1} and α_c = -10.5 × 10^{-6} K^{-1} for the H phase and α_a = 11.1 × 10^{-6} K^{-1} for the α phase (110-430 K) (The lattice constants are refined from the full-profile fitting patterns for 5Tb at different temperatures using SXRD data, see Supplementary Table 1 and Supplementary Figure 7).

The hexagonal H phase shows NTE in the LD and the body cubic center α phase shows PTE, so tuning the phase contents in the samples could control the CTEs of dual-phase alloys. Therefore, the macroscopic thermal expansion curves (ΔL/L0) of these dual-phase alloys were measured using a dilatometer, as shown in Figure 4. The CTE along the LD can be tuned from positive (α_l = 6.0 × 10^{-6} K^{-1} for 2.5Tb alloy and α_l = 4.0 × 10^{-6} K^{-1} for 2Er alloy) to negative (α_l = -4.9 × 10^{-6} K^{-1} for 7.5Tb alloy and α_l = -15.7 × 10^{-6} K^{-1} for 9Er alloy) with gradually increasing Tb/Er content in dual-phase alloys (see Figure 4A and B). Among these alloys, both 5Tb and 4Er alloys exhibit axial ZTE along LD over a temperature range involving room temperature (α_l = 0.029 × 10^{-6} K^{-1}, 110 to 425 K for 5Tb alloy, α_l = -0.33 × 10^{-6} K^{-1}, 110 to 330 K for 4Er alloy). The temperature ranges of ZTE for 5Tb and 4Er alloys are consistent with the changes of their macroscopic magnetic properties (see Supplementary Figure 6). Meanwhile, the linear thermal expansion curves of 5Tb and 4Er along the TD-ND plane confirmed normal PTE in other directions (see Figure 4C). Both 5Tb and 4Er alloys show normal PTE in the TD-ND plane (α_l = 6.72 × 10^{-6} K^{-1}, 110 to 425 K for 5Tb alloy, α_l = 6.56 × 10^{-6} K^{-1}, 110 to 330 K for 4Er alloy), i.e., exhibiting the LZTE behavior. This finding is consistent with the result of variable temperature SXRD shown in Figure 3I: α_c = -1.7 × 10^{-6} K^{-1}, and α_a = 6.4 × 10^{-6} K^{-1}, 110-430 K. (Because the EBSD IPF verifies the existence of crystallographic texture along the LD for both the H and α phases ($[001]_H//[111]_\alpha$//LD), the average "lattice" thermal expansion of 5Tb in the LD and TD-ND plane can be calculated by $L(a) = a(\alpha) \times$ mol. α % + a(H) × mol. H % and $L(c) = c(\alpha) \times$ mol. α %+c(H) × mol. H %).

In order to verify the thermal circulation stability of 5Tb and 4Er alloys with LZTE performance, a thermal cycling test was carried out by switching between 77 and 373 K (see Figure 4D). The CTE variations of both alloys are negligible after hundreds of thermal cycling ($\Delta\alpha_l$ = -0.16 × 10^{-6} K^{-1} for 5Tb alloy and $\Delta\alpha_l$ = -0.69 × 10^{-6} K^{-1} for 4Er alloy after 100 times of thermal cycling, $\Delta\alpha_l$ = -0.31 × 10^{-6} K^{-1} for 5Tb alloy and $\Delta\alpha_l$ = -0.81 × 10^{-6} K^{-1} for 4Er alloy after 200 times of thermal cycling). As shown in the TEM and HRTEM images (see Figure 4E and F), such excellent thermal circulation stability of 5Tb and 4Er alloys is a benefit from the formation of a firm and natural phase boundary between the αand H phases due to the hypo-eutectic reaction process. It gives rise to a natural dual-phase structure that maintains perfect integrity under thermal cycling that greatly elevates the application potential under intense temperature changes[20].

The mechanical property is critical for LZTE alloys because most LZTE alloys suffer from severe brightness. Figure 5 demonstrates the engineering stress-strain curves along the LD of the 5Tb and 4Er alloys under compressive conditions. They manifest that the ultimate compressive stress (δ_{US}) reaches 0.80 GPa with a strain of 3.9% for the 5Tb alloy and 0.73 GPa with a strain of 13.8% for the 4Er alloy. Figure 5C proves that the mechanical and thermal expansion properties of the two alloys exceed most known LZTE alloys[20,28,30-36] and that moderate plasticity and strength make the LZTE alloys easily machined. The SEM images of the fractured surface of the 5Tb alloy are shown in Figure 5D and E. It is seen that the fractured α phase is dispersed in the cracked matrix of the H phase, suggesting that the plastic α phase hinders the enlargement

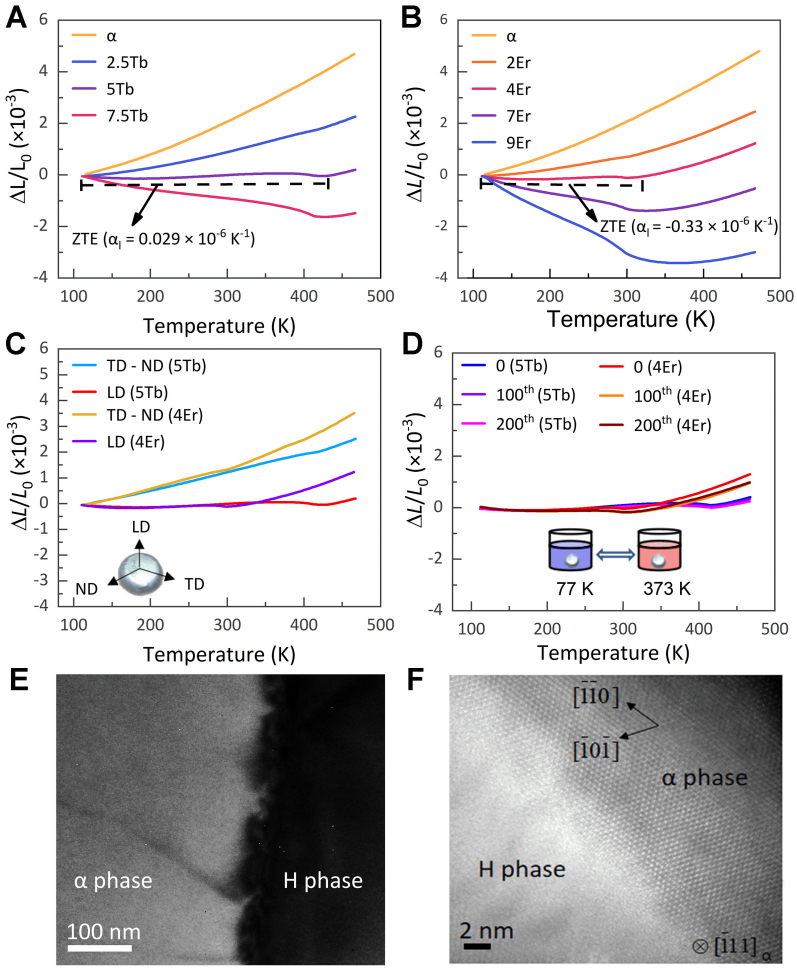

Figure 4. Dilatometric thermal expansion behaviors and TEM images of the 5Tb alloy. (A) The thermal expansion curves of 2.5Tb, 5Tb, and 7.5Tb alloys and pure iron along the LD. (B) The thermal expansion curves of 2Er, 4Er, 7Er, and 9Er alloys and pure iron along the LD. (C) The thermal expansion curves along LD, TD- ND plane for 5Tb alloy and 4Er alloy. (D) The thermal expansion curves of 5Tb alloy and 4Er alloy along the LD under the thermal cycling between 77 and 373 K. (E and F) The transmission electron microscope (TEM) (E) and high-resolution transmission electron microscope (HRTEM). (F) of the interface structure between the H and α phases.

of cracks in the H phase during compressing test[20,37,38]. On the other hand, because the H phase is the matrix of a dual-phase alloy, the high strength of this phase is retained in the LZTE alloy (see Figure 3A). Hence, 5Tb and 4Er alloys - two novel LZTE dual-phase alloys with a desired combination of plasticity and strength were obtained, which satisfied the design principle shown in Figure 1. Moreover, moderate plasticity and strength make the LZTE alloys easily machined (see Figure 5E), and the high Fe contents of LZTE alloys make them low-cost.

CONCLUSION

In summary, it was shown that a phase fraction tuning design of optimizing the compositions of alloys and hypo-eutectic reactions yields two types of novel LZTE dual-phase alloys, $Tb_{0.05}Fe_{0.95}$ and $Er_{0.04}Fe_{0.96}$. Both alloys are characterized by high mechanical properties, thermal circulation stability, machinability, and LZTE effect over a wide temperature range including room temperature. The crystallographic texture of H and α phases in the LD and the appropriate phase ratios result in the LZTE of the $Tb_{0.05}Fe_{0.95}$ and $Er_{0.04}Fe_{0.96}$ alloys. The plastic α phase dispersed in the H phase improves the plasticity of the dual-phase alloy by

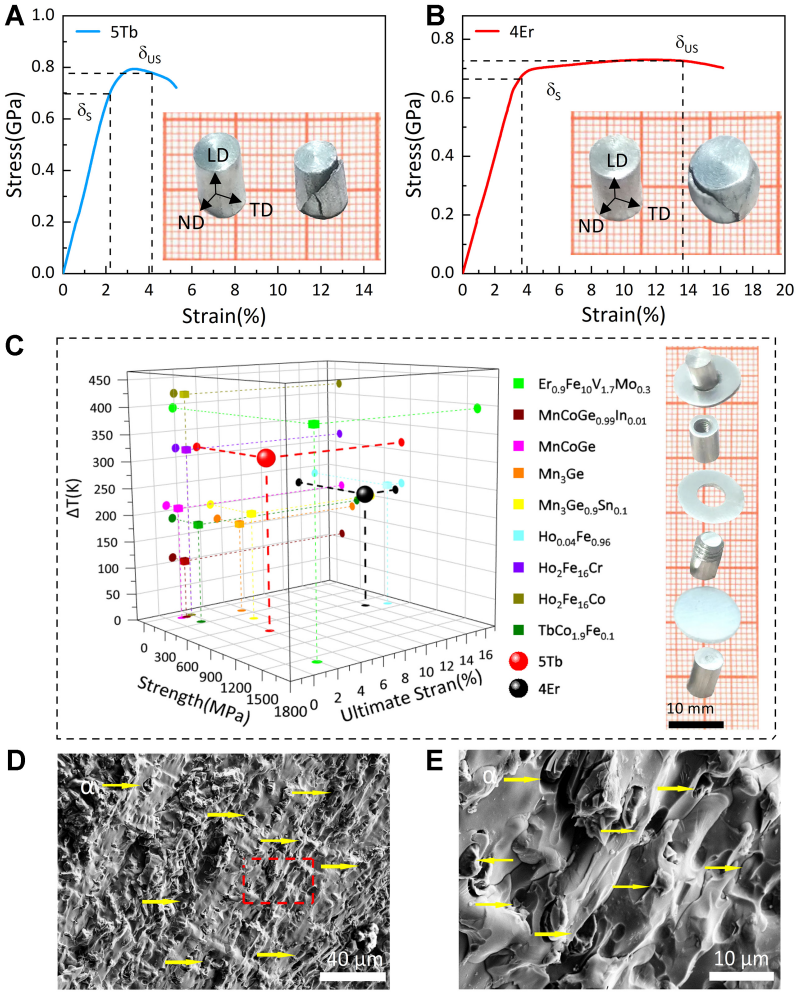

Figure 5. Mechanical properties. (A and B) Engineer compressive stress-strain curves of 5Tb alloy (A) and 4Er alloy (B) with the inset ingots, respectively, along the LD during loading. (C) The Ashby-type plot for the typical LZTE alloys: ultimate strain, strength, and temperature window, and the mechanically machined components of 5Tb and 4Er alloys are on the right side. (D) SEM image of the fractured 5Tb ingot surface. (E) The enlarged region in (D) is signed with a red rectangle.

hindering the crack propagation inside the H phase under compression. Besides, the dual-phase alloys retain high strength because the H phase is the matrix of the dual-phase alloys. Such comprehensive properties of $Tb_{0.05}Fe_{0.95}$ and $Er_{0.04}Fe_{0.96}$ alloys are scarce in LZTE alloys, which could have a broad application foreground.

DECLARATIONS

Acknowledgments

The synchrotron radiation experiments were approved by the Japan Synchrotron Radiation Research Institute (JASRI) (Proposal No. 2023A1269, 2023A1849, 2024A1556) and were conducted on BL02B2 and BL44B2 of SPring-8.

Authors' contributions

Experimental design, data analysis: Su J, Lin K, Yu C

Sample synthesis, material testing, original manuscript writing: Su J, Miao J, Cao Y
Validation and original manuscript writing: Su J, Lin K, Li Q, Xing X
All authors have read and agreed to the published version of the manuscript.

Availability of data and materials

The data that support the findings of this study are available from the corresponding author upon reasonable request.

Financial support and sponsorship

This research was supported by the National Key R&D Program of China (2020YFA0406202), National Natural Science Foundation of China (22371014, 22090042 and 21971009), Guangxi BaGui Scholars Special Funding (2019M660446), and Fundamental Research Funds for the Central Universities, China (FRF-EYIT-23-03, GJRC2023003).

Conflicts of interest

All authors declared that there are no conflicts of interest.

Ethical approval and consent to participate

Not applicable.

Consent for publication

Not applicable.

Copyright

© The Author(s) 2024.

REFERENCES

1. Chippindale AM, Hibble SJ, Bilbé EJ, et al. Mixed copper, silver, and gold cyanides, $(M_xM'_{1-x})CN$: tailoring chain structures to influence physical properties. *J Am Chem Soc* 2012;134:16387-400. DOI
2. Guo J, Fu S, Deng Y, et al. Hypocrystalline ceramic aerogels for thermal insulation at extreme conditions. *Nature* 2022;606:909-16. DOI PubMed PMC
3. Ha CS, Plesha ME, Lakes RS. Simulations of thermoelastic triangular cell lattices with bonded joints by finite element analysis. *Extreme Mech Lett* 2017;12:101-7. DOI
4. Hu P, Chen J, Sun X, et al. Zero thermal expansion in $_{(1-x)}PbTiO_{3-x}Bi(Mg,Ti)_{1/2}O_3$ piezoceramics. *J Mater Chem* 2009;19:1648-52. DOI
5. Jiang X, Molokeev MS, Gong P, et al. Near-zero thermal expansion and high ultraviolet transparency in a borate crystal of $Zn_4B_6O_{13}$. *Adv Mater* 2016;28:7936-40. DOI
6. Kumar PS, Kini NS, Umarji AM, Sunandana CS. Search for a novel zero thermal expansion material: dilatometry of the AgI-CuI system. *J Mater Sci* 2006;41:3861-5. DOI
7. Lehman J, Lakes R. Stiff lattices with zero thermal expansion and enhanced stiffness via rib cross section optimization. *Int J Mech Mater Des* 2013;9:213-25. DOI
8. Loring KJ, Ortega LF, Monroe JA, et al. Hydroxide catalysis bonding of Allvar alloy 30, a negative thermal expansion alloy. *J Astron Telesc Instrum Syst* 2020;6:015007. DOI
9. Monroe JA, East M, Hull T. ALLVAR alloy athermalization: a novel and cost-effective alternative for small to moderate sized space telescopes. *Soc Photo Opt Instrum Eng* 2021;11820:118200B. DOI
10. Monroe JA, McAllister JS, Content DS, Zgarba J. Negative thermal expansion ALLVAR alloys for smaller optics. *Soc Photo Opt Instrum Eng* 2020;11310:1131013. DOI
11. Kulkarni S, Umińska AA, Sanjuán J, et al. Characterization of dimensional stability for materials used in ultra-stable structures. *Soc Photo Opt Instrum Eng* 2021;11820:1182008. DOI
12. Monroe JA, McAllister JS, Content DS, Zgarba J, Huerta X, Karaman I. Negative thermal expansion ALLVAR alloys for telescopes. *Soc Photo Opt Instrum Eng* 2018;10706:107060R. DOI
13. Zhao Y, Huang R, Li S, et al. Giant isotropic magnetostriction in $NaZn_{13}$-type $LaFe_{13-x}Al_x$ compounds. *Appl Phys Lett* 2017;110:011906. DOI

14. Lehman J, Lakes R. Stiff, strong zero thermal expansion lattices via the Poisson effect. *J Mater Res* 2013;28:2499-508. DOI
15. Chen R, Zhu Y, Chen L, et al. A near-zero thermal expansion material: $AlMoVO_7$. *Chem Phys Lett* 2021;769:138425. DOI
16. Iwai Y, Nakaya M, Ohtsu H, Le Ouay B, Ohtani R, Ohba M. Zero area thermal expansion of honeycomb layers *via* double distortion relaxation in $(PPh_4)[Cu_2(CN)_3]$. *CrystEngComm* 2022;24:5880-4. DOI
17. Jiang X, Wang N, Dong L, et al. Integration of negative, zero and positive linear thermal expansion makes borate optical crystals light transmission temperature-independent. *Mater Horiz* 2022;9:2207-14. DOI
18. Liu Z, Yang J, Yang L, et al. Argentophilicity induced anomalous thermal expansion behavior in a 2D silver squarate. *Inorg Chem Front* 2021;8:1567-73. DOI
19. Yu C, Lin K, Cao Y, et al. Two-dimensional zero thermal expansion in low-cost $Mn_xFe_{5-x}Si_3$ alloys via integrating crystallographic texture and magneto-volume effect. *Sci China Mater* 2022;65:1912-9. DOI
20. Lin K, Li W, Yu C, et al. High performance and low thermal expansion in Er-Fe-V-Mo dual-phase alloys. *Acta Mater* 2020;198:271-80. DOI
21. Yu C, Lin K, Jiang S, et al. Plastic and low-cost axial zero thermal expansion alloy by a natural dual-phase composite. *Nat Commun* 2021;12:4701. DOI PubMed PMC
22. Zhang H, Xing C, Zhou H, et al. Giant anisotropic magnetocaloric effect by coherent orientation of crystallographic texture and rare-earth ion moments in HoNiSi ploycrystal. *Acta Mater* 2020;193:210-20. DOI
23. Özbilgin CE, Kobayashi K, Tamura S, Imanaka N, Suzuki TS. Anisotropic thermal expansion and ionic conductivity of a crystal-oriented, Mg^{2+} - conducting NASICON-type solid electrolyte. *Ceram Int* 2022;48:10733-40. DOI
24. Shan X, Huang R, Han Y, Huang C, Li L. Preparation and property study of $La(Fe, Si, Co)_{13}$/Cu composite with nearly zero thermal expansion behavior. *J Alloys Compd* 2015;648:463-6. DOI
25. Zhou H, Tao K, Chen B, et al. Low-melting metal bonded MM′X/In composite with largely enhanced mechanical property and anisotropic negative thermal expansion. *Acta Mater* 2022;229:117830. DOI
26. Yang Z, Zhang Y, Zhang Z, Liu S. Buckling enhancement of tubular metamaterial with axial zero thermal expansion by integrating two adjustment mechanisms. *Mater Res Express* 2022;9:045801. DOI
27. Li L, Gong Y, Wang C, Zhang Y, Xu F. Achievement of zero thermal expansion covering room temperature in the $La(Fe,Al)_{13}$-based bulks with reduced annealing time. *Phys B Condens Matter* 2022;636:413897. DOI
28. Cao Y, Lin K, Khmelevskyi S, et al. Ultrawide temperature range super-invar behavior of $R_2(Fe,Co)_{17}$ materials (R = rare earth). *Phys Rev Lett* 2021;127:055501. DOI
29. Rong MH, Chen XL, Wang J, Rao GH, Zhou HY. Thermodynamic re-assessment of the Fe-Dy and Fe-Tb binary systems. *Calphad* 2017;59:154-63. DOI
30. Zhao YY, Hu FX, Bao LF, et al. Giant negative thermal expansion in bonded MnCoGe-based compounds with Ni_2In-type hexagonal structure. *J Am Chem Soc* 2015;137:1746-9. DOI
31. Yu C, Lin K, Zhang Q, et al. An isotropic zero thermal expansion alloy with super-high toughness. *Nat Commun* 2024;15:2252. DOI PubMed PMC
32. Wang J, Gong Y, Liu J, et al. Balancing negative and positive thermal expansion effect in dual-phase $La(Fe,Si)_{13}$/α-Fe in-situ composite with improved compressive strength. *J Alloys Compd* 2018;769:233-8. DOI
33. Song Y, Qiao Y, Huang Q, et al. Opposite thermal expansion in isostructural noncollinear antiferromagnetic compounds of Mn_3A (A = Ge and Sn). *Chem Mater* 2018;30:6236-41. DOI
34. Song Y, Chen J, Liu X, et al. Zero thermal expansion in magnetic and metallic $Tb(Co,Fe)_2$ intermetallic compounds. *J Am Chem Soc* 2018;140:602-5. DOI
35. Liu J, Gong Y, Wang J, et al. Realization of zero thermal expansion in $La(Fe,Si)_{13}$-based system with high mechanical stability. *Mater Des* 2018;148:71-7. DOI
36. Dan S, Mukherjee S, Mazumdar C, Ranganathan R. Zero thermal expansion with high Curie temperature in $Ho_2Fe_{16}Cr$ alloy. *RSC Adv* 2016;6:94809-14. DOI
37. Ying H, Yang X, He H, et al. Formation of strong and ductile FeNiCoCrB network-structured high-entropy alloys by fluxing. *Microstructures* 2023;3:2023018. DOI
38. Xu N, Huang Y, Cao Y, Li S, Wang Yd. Novel casting CoCrNiAl eutectic high entropy alloys with high strength and good ductility. *Microstructures* 2023;3:2023015. DOI